Low threshold acquisition controller for Skipper charge-coupled devices

Gustavo Cancelo,[a] Claudio Chavez,[b] Fernando Chierchie,[c] Juan Estrada,[a] Guillermo Fernandez Moroni,[a,c,*] Eduardo Paolini,[c,d] Miguel Sofo Haro,[e] Angel Soto,[c] Leandro Stefanazzi,[a,c] Javier Tiffenberg,[a] Ken Treptow,[a] Neal Wilcer,[a] and Ted Zmuda[a]

[a]Fermi National Accelerator Laboratory, Batavia, Illinois, United States
[b]Universidad Nacional de Asunción, Facultad de Ingeniería, Paraguay, Asunción, Paraguay
[c]Universidad Nacional del Sur, Instituto de Investigaciones en Ingeniería Eléctrica "Alfredo C. Desages" (IIIE-CONICET), Departamento de Ingeniería Eléctrica y de Computadoras, Bahía Blanca, Argentina
[d]Comisión de Investigaciones Científicas Prov. Buenos Aires, Buenos Aires, Argentina
[e]Universidad Nacional de Cuyo, Centro Atómico Bariloche and Instituto Balseiro, Comisión Nacional de Energía Atómica, Rio Negro, Argentina

Abstract. The development of the Skipper-charge-coupled devices (Skipper-CCDs) has been a major technological breakthrough for sensing very weak ionizing particles. The sensor allows to reach the ultimate sensitivity of silicon material as a charge signal sensor by unambiguous determination of the charge signal collected by each cell or pixel, even for single electron–hole pair ionization. Extensive use of the technology was limited by the lack of specific equipment to operate the sensor at the ultimate performance. A simple, single-board Skipper-CCD controller designed by the authors is presented and aimed for the operation of the detector in high sensitivity scientific applications. Our article describes the main components and functionality of the so-called low threshold acquisition controller together with experimental results when connected to a Skipper-CCD sensor. Measurements show unprecedented deep subelectron noise of 0.039 e^-_{rms}/pix by nondestructively measuring the charge 5000 times in each pixel. [DOI: 10.1117/1.JATIS.7.1.015001]

Keywords: CCD controller; Skipper-CCD; charge-coupled device; sub-electron noise.

Paper 20067 received Jun. 12, 2020; accepted for publication Dec. 16, 2020; published online Jan. 21, 2021.

1 Introduction

Although charge-coupled devices (CCDs) were invented as memory devices in the 1970s,[1,2] they have proven to be very powerful for detecting photons and other particles that interact with silicon atoms.[3] The number of applications is still growing.[4–8]

For photon detection, CCD sensors rely on the photoelectric effect to absorb incident photons in a silicon substrate and generate electron–hole (e–h) pairs.[3] Energetic photons ($E > 10$ eV) produce multiple e–h pairs allowing an energy measurement.[9] Instead, lower energy photons may only generate one or very few e–h pairs. Massive particles can also create e–h pairs either by directly interacting with valence-band electrons or by scattering off silicon nuclei. For these reasons, CCDs are not only used for optical applications but also for applications in nuclear physics and cosmology.

Most CCDs used in instruments, such as cameras for astronomy and cosmology, require a high dynamic range. The CCD pixels collect the ionized charge generated by interacting photons coming from objects in the front of sight during a certain exposure time. That signal may amount to a few hundred thousand electrons or holes (i.e., depending on the CCD type). Other applications in science and industry, such as searches for dark matter and the coherent neutrino

*Address all correspondence to Guillermo Fernandez Moroni, fmoroni.guillermo@gmail.com

2329-4124/2021/$28.00

scattering, or neutron and quantum imaging, to name a few, are interested in faint signals, as small as 1 e–h pair. Henceforth, CCD dynamic range, pixel readout time, and readout noise are application specific. However, independent of the application, precision measurements are limited by the readout noise of the CCD readout electronics. Other sources of measurement ambiguity, such as dark current, are extremely low (e.g., 10^{-9} $e^-/pix/s$, where e^- is the typical unit used to account for the number of carriers collected) when the CCD is operating at low temperatures (e.g., 140 K). Furthermore, charge transfer efficiency can be as good as 99.9999%.

Recently, Tiffenberg et al.[10] have successfully used a Skipper-CCD to overcome the 2 e^- noise limit of standard CCDs approaching noise levels of 0.068 e^- root mean square (rms). A Skipper-CCD has an extra charge storage that allows multiple nondestructive measurements of the same pixel charge to be averaged in an uncorrelated fashion, breaking the $1/f$ dependence. At this noise level, the CCD becomes an e–h pair counter with an error probability of $\sim 10^{-13}$. This Skipper-CCD designed by Steve Holland at Lawrence Berkeley National Laboratory (LBNL) is the first accurate single-electron counting silicon detector on a large footprint. The performance of the first device was published in Ref. 11. The Skipper-CCD also has linear gain, which allows to readout charge packets of thousands of electrons with the same noise level. As pointed out in Ref. 10, that makes the Skipper-CCD the most sensitive and robust electromagnetic calorimeter that can operate at temperatures above that of liquid nitrogen. It also allows the Skipper-CCD to count individual optical and near-infrared photons. CCDs with subelectron readout noise have a broad range of applications including particle physics (e.g., ultralow-noise searches for dark matter and neutrinos) and astronomy (e.g., direct imaging and spectroscopy of exoplanets). The price to be paid for achieving such an outstanding noise level is the total readout time. The 0.1 e^- rms reported in Ref. 10 takes an average of 1200 reads of the same pixel charge using a pixel readout time of 10 μs for a noise of 3.5 e^-/sample. That totals 12 ms/pixel at 0.1 e^- of noise. Even for applications that are not time critical, the readout time of a large device can become a problem due to other on-chip exposure-dependent noise source as dark current. In the following sections of this paper, we show that the noise-time performance of the Skipper-CCD can be improved by the CCD readout. The reason for this improvement is simple. Readout electronics have been unable to attend the noise limit of the CCD video output. There is still room for a cleaner electronics that lowers the dual slope integrator (DSI) noise integrated over a unit of time. A typical readout electronics also controls the charge sequencing out of the CCD and generates the bias voltages needed for operation. Both tasks introduce an excess noise into the CCD that adds to the intrinsic noise of the video signal path. The noise problem is analyzed in Sec. 3.

Until now, the high sensitivity to small energy depositions of the Skipper sensors could not be exploited in scientific or technological applications, due to the lack of scientific grade equipment to operate them. Previous works with the sensor[10,11] were reported using modified existing electronics, such as the Monsoon controller[12,13] or the controllers developed by Leach et al.[14–16] in extremely well-controlled experiments and without the possibility to scale or duplicate the system. The low threshold acquisition (LTA) readout electronics presented in this work is specifically designed to meet the requirements on this new scenario of the growing demand of the technology. The group has large experience working with Skipper-CCD sensors and is currently leading cutting edge applications. Due to the compact design, the ease of fabrication, operation, and noise performance, the LTA has already proven to be the solution for many groups working or willing to work with Skipper-CCDs. Among these applications, we can cite: leading light dark matter searches currently being used in the Sub-Electron-Noise Skipper-CCD Experimental Instrument (SENSEI);[6] next generation of the Dark Matter in CCDs experiment for dark matter searches;[17,18] part of the R&D program of the OSCURA project, a 10-kg active silicon experiment for dark matter detection based on Skipper-CCDs; next generation of reactor neutrino detection such as the Coherent Neutrino–Nucleus Interaction Experiment;[7,19] new spectrograph instruments;[10] new single photon counting quantum imaging cameras; new program for high procession silicon property measurements (quenching factor, Fano factor, ionization energy distribution, and temperature dependence);[20,21] cold neutron quantum measurements;[22] and construction of large Skipper-CCD testing labs.[23]

The paper is organized as follows: a description of the LTA system is presented in Sec. 2. A theoretical framework for the readout noise analysis in Skipper-CCD is given in Sec. 3. Then, measurements of the performance of the controller disconnected from the CCD are presented

in Sec. 4 and operation with a sensor in Sec. 5. Finally, some remarks and conclusions are presented in Sec. 6.

2 Low Threshold Acquisition Controller

2.1 *Hardware*

The LTA is a single printed circuit board hosting four video channels for readout, plus CCD bias, and control signals. It has been optimized to work with the p-channel, thick, high resistivity CCDs, such as the ones described in Ref. 24. A block diagram of the LTA is given in Fig. 1. Video channels are built using tightly coupled low-noise differential amplifiers (LTC6363) and 18-bit, 15-Msps analog-to-digital converters (ADC) (LTC2387) to capture the video signals, and digital dual slope integrator (DDSI) is implemented to compute the pixels values. A detailed characterization and description of the performance of the former ADC applied for CCD readout can be found in Ref. 25. For a preamplifier gain of 4 to allow a large input dynamic range, the input noise floor of the LTA is -145 dBFS/Hz.

The heart of the LTA is a Xilinx Artix XC7A200T field programmable gate arrays (FPGA). The FPGA is in charge of setting up the programmable bias voltages, managing the clock signals that transport the pixel charge along the CCD array, video acquisition, telemetry, and the transmission of data from the board to the personal computer (PC). The fully digital approach on the data path brings the advantage of digital signal processing techniques for noise reduction on the video channels. This feature of the LTA board has been previously explored in Refs. 23 and 26, where optimal filters with a better signal-to-noise ratio (SNR) than DDSI. More about the FPGA firmware can be found in Sec. 2.2.

The CCD clocks are generated by a 40-channel digital-to-analog converter (DAC) (AD5371), analog switches (ADG5234), and Op Amps (THS6072). The DAC is used as a multi-channel adjustable potentiometer. It allows setting clock values of up 20 V of dynamic range within ± 15 V. The voltage range is controllable by an internal offset. Each CCD clock uses two DAC outputs to define its low and high states. The analog switches are used to generate the clock signals switching between the low and high voltages of each clock. As shown in Fig. 1, the operational amplifiers and associated *R-C* network provide the desired rise and fall time. The clock shaping and the output noise in these lines are critical, CCD clocking signals with voltage swings of up to 10 volts and $\mathrm{d}V/\mathrm{d}t$ on the order 50 V/μs are typical and induce crosstalk on the video lines. Although clocks remain stable during the video readout, some noise from clock feed-through may still be present during DSI integration times. That is not white Gaussian noise (WGN), so minimizing it at the generation point on the LTA board is of paramount importance.

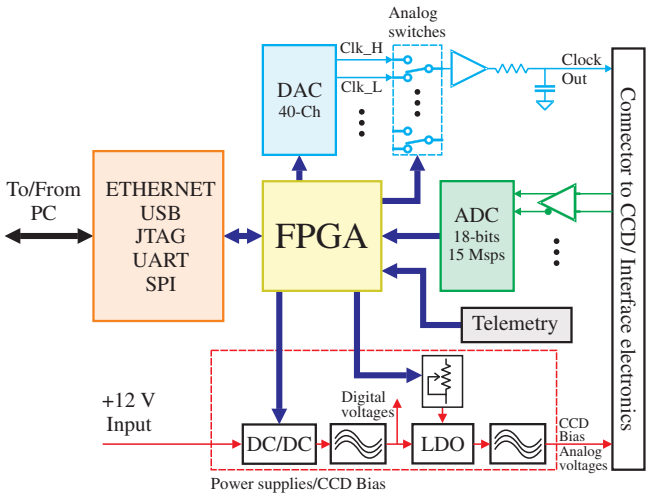

Fig. 1 Block diagram of the main hardware components in the LTA.

Coupling of 1 ppm from a 10-V clock into the video has already a considerable negative impact on the noise.

Another critical part of the LTA is the power generation and management. This block is shown in Fig. 1 inside a dashed box. The LTA is a 7×8 in.^{2} single board CCD readout and control (Fig. 2). A design of this kind requires many dc voltages to power digital and analog components. Furthermore, the CCD requires several dc bias voltages that must be as clean of noise as possible and have the flexibility of being adjusted for performance optimization. The LTA only requires an input power source of $+12$ V dc. Although we have not noticed any negative increase of noise using a standard ac/dc switching supply, it is important to keep the input voltage clean[27] and to avoid high-frequency switching noise. That noise couples to the output of either linear or switching ac/dc supplies or could be intermodulated to lower frequencies.

The dc switchers (LT3580) are operated at 2 MHz to keep switching noise away from the frequency band of interest for CCD readout. Since CCD bias are negative, we used the ultralow noise TPS7A33 with input and output filtering, achieving 100 μV rms of output noise. This new series of ultralow noise regulators is critical in minimizing the noise that couples to the video inputs on board and the noise that couples to the CCD and cables. This topic is expanded in Sec. 3.

The CCD bias voltages are adjustable through AD5293 digitally controlled potentiometers. The power of other noise-sensitive analog electronics, such as the ADC and the video preamplifier, is based on a combination of a LT3580 dc/dc switcher and the LT3045 ultralow noise linear regulator.

Special consideration has been taken with the CCD substrate bias V_{sub}, which is controllable up to $+100$ V. The dc/dc converter uses an external voltage multiplier made with discrete components (i.e., diodes, capacitors, and resistors). The output of the switcher is filtered by another ultralow noise linear regulator TPS7A4001. Moreover, this hardware was designed to allow the implementation of the "erase" procedure of the CCDs, in which V_{sub} is varied in a controlled way to reduce dark current and to remove ghost images.[24,28]

All power supplies and voltages default to strategic voltages at power up, and they are controlled and sequenced by the FPGA. All clock and bias voltages are accessible through the

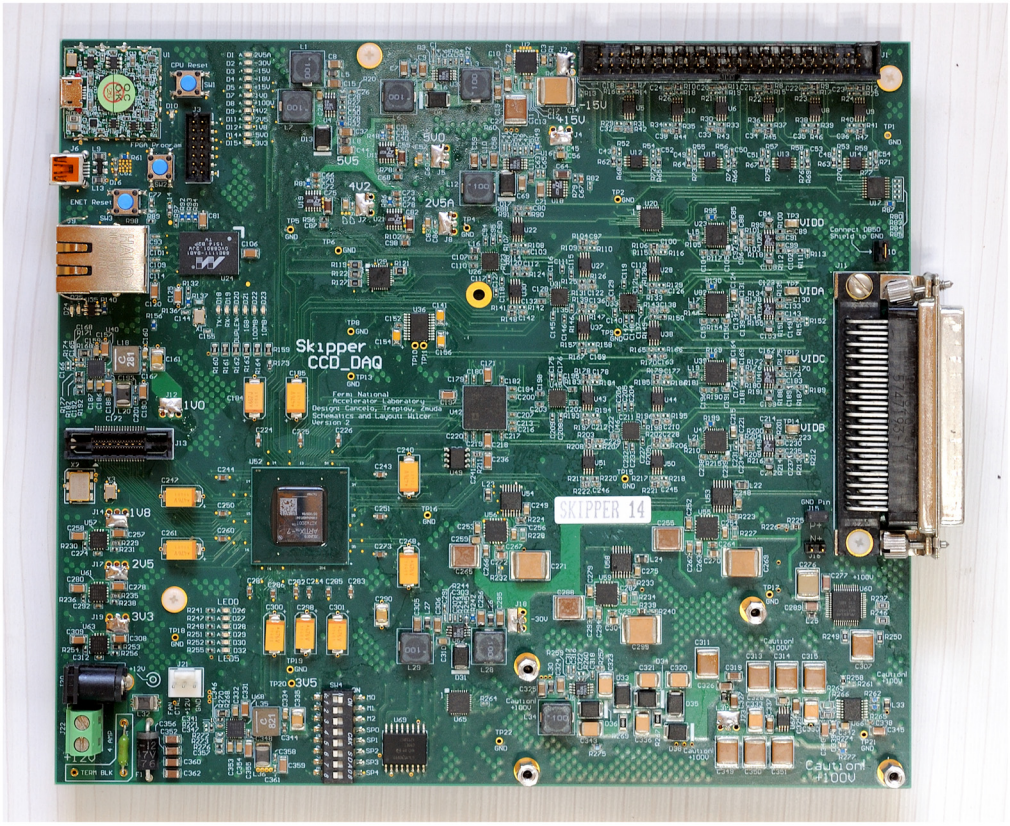

Fig. 2 LTA electronics.

telemetry system based on a AD7328 12-bit ADC and analog multiplexers. Also, a header connector on the board allows manual debugging of clock and bias signals through instrumentation, such as an oscilloscope or logic state analyzer. The signals going to the header connector are buffered to prevent potential damage caused by the external instrumentation. In addition to the high-speed gigabit Ethernet interface, the board has USB (universal serial bus), UART (Universal Asynchronous Receiver–Transmitter), SPI (Serial Peripheral Interface), JTAG (Joint Test Action Group) interfaces for debugging purposes and FPGA programming. After debugging, the firmware resides on an on-board Flash NVRAM (non-volatile random-access memory) and automatically boots up at power up.

The board also has dedicated hardware to synchronize many boards together in master-slave mode to build multiple CCD systems.

2.2 *Firmware*

The user interacts with the board through a single Ethernet port, which allows sending and receiving commands as well as data. Serial interface is reserved for debugging purposes. A block diagram of the main units and control flow of the firmware on the FPGA is shown in Fig. 3. The initial setup and the slow speed control of all the blocks are driven by a soft-core μBlaze processor. The software is a stand-alone, lightweight application developed in C-language, requiring not more than 256 kBytes of memory, which allows the use of internal FPGA memory.

Precise timing is required to control the clock signals of the CCD. To this end, the sequencer (Seq) module is implemented in hardware to ensure precise synchronization of clock signals and ADC samples processing during the CCD readout. In normal operation, ADC samples are fed into the DDSI block, which computes the average of the samples, the pixel integration time is controlled by the sequencer.

In normal operation, the pixel information coming out of the DSI block is wrapped with extra control information in the Packer module and sent to the Ethernet module for external transmission. Clocks and bias modules control the configuration of clocks and bias voltages, and the "Tele" module is in charge of the telemetry information collection from clocks and biases voltages. The LTA also allows for easy scaling to any number of CCDs operated in parallel. For this purpose, the boards are connected together and configured in slave mode. Only one of them runs in master mode providing synchronization of the CCD clock sequence for the entire group. A synchronized readout avoids extra noise from cross-talk noise from clocks transitions.

A special firmware module, called the "smart buffer" was added for CCD-systems debugging purposes. This block can store 65536 ADC samples at 15 MHz with 18-bits. Signals from the sequencer are routed to the buffer and are used like external triggering, allowing to store ADC samples at very precise moments. The LTA can store in this buffer the raw video signal (hundreds of raw samples per pixel) for hundreds of pixels (depending on the pixel time). For example, for a total pixel time of 30 μs, 450 raw ADC samples are taken for each pixel, and a total of $65536/450 = 145$ pixels are stored in the smart buffer. These raw samples are sent to the

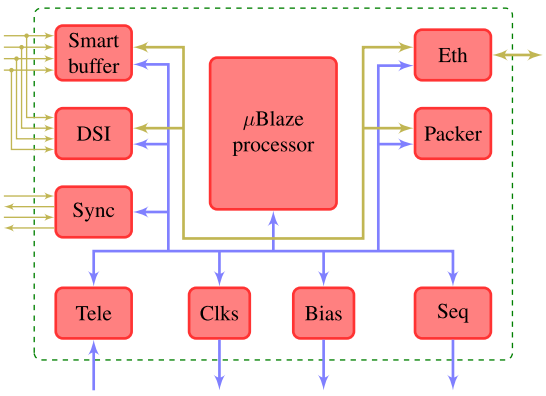

Fig. 3 Details of the FPGA firmware with low-speed control AXI bus (blue lines) and high throughput data paths (brown lines).

computer afterward and a csv file is created. This module is useful to analyze and debug problems with a CCD system. It can be used as a remotely controlled oscilloscope, the user can configure it to capture one or more raw video channels, to optimize readout speed, noise performance, or to detect problems in the video chain.

JTAG port connectivity is added for easy programming and debugging. Nonvolatile 512 MB flash memory provides location to store the FPGA bit-stream for permanent, non-JTAG functioning.

2.3 *Software*

LTA software is written in C++ with open-source libraries for internet protocol (IP) communications. It is based on a client-server model where a local daemon provides services for commands, telemetry, and data acquisition. Users interact with the software using a request-response method through the terminal to perform LTA board configuration, readout, and telemetry requests and also sequencer uploading.

Data and commands are transmitted entirely using user datagram protocol, over IP through the computer giga-etherner port and the software relies on the hard-drive as buffer to avoid unnecessary RAM usage. At the end of data acquisition, the software performs a coherency check and delivers final images in FITS (Flexible Image Transport System) and other formats.

The code has been designed for easy compilation on Linux distributions operating systems and has been already tested in Ubuntu, Scientific Linux, Centos, Rasp-bian, Ubuntu over WSL (Windows Subsystem for Linux), and Open Suse over WSL. With few modifications, it can run over other Linux distributions.

3 Theoretical Noise Framework

3.1 *Noise Sources*

The CCD sensor and its associated control and readout electronics constitute a tightly coupled system. The total readout noise is a combination of all noise sources along the readout chain. That chain starts with the internal CCD readout MOSFET (metal–oxide–semiconductor field-effect transistor), continues with an interface electronics for preamplification, and finishes with the data acquisition and video signal processing. Noise from control and bias signals will couple to the CCD internal readout and also along the cabling (e.g., CCD package, flex cables, etc.). Since all control and bias signals are highly coupled to the video signal, they are potential noise sources. Figure 4 summarizes the main noise sources to be considered. Three noise sources are included, the $V_{\text{noise}}^{\text{bias}}$ source models the noise present in the bias voltages, which are generated by the readout electronics; the $V_{\text{noise}}^{\text{clock}}$ is the noise present in the clocking signals, which are also generated in the readout electronics; finally, the $V_{\text{noise}}^{\text{video}}$ models the noise introduced by the built-in

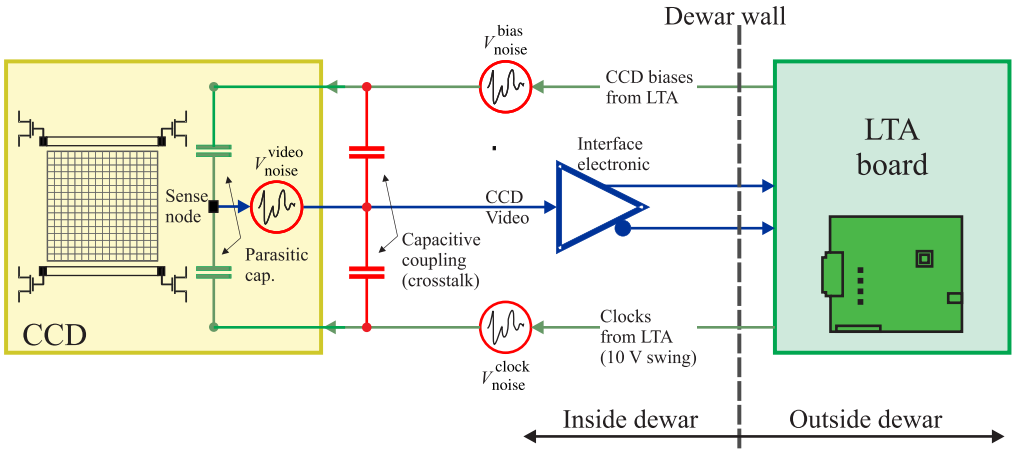

Fig. 4 Noise sources' block diagram.

CCD output transistor amplifier. Minimizing the control and bias signal noise and the additive noise from external amplification stages is extremely important and allows to get the lowest uncertainty limit given by the built-in output transistor of the sensor. Figure 4 also illustrates the couplings that exist internally in the CCD (green capacitors) and externally in the cables (red capacitors). The readout technique should be studied to evaluate the effect on the noise source and then normalize it by a calibration gain to convert it to physical units. A theoretical overview of these aspects is detailed in the next sections.

3.2 *Digital Dual Slope Integrator*

Since the CCD pixel array is read out serially through one or more output amplifiers, the amplifier's noise is added to the charge of each pixel.[3] The readout method to achieve lower noise is integration. If we assume that most of the noise energy is white and Gaussian, we obtain a noise reduction proportional to the square root of the integration time. Furthermore, as most integrators require a reset, a pixel baseline (known as the pedestal level) is needed, which comes with a time penalty of equal integration time. That readout method, widely called DSI,[3] is described by the following equation:[3]

$$P_i = \frac{A}{t_{i,\mathrm{DSI}}}\left(\int_{t_{i,\mathrm{DSI}}+\tau}^{2t_{i,\mathrm{DSI}}+\tau} x(t)\mathrm{d}t - \int_{0}^{t_{i,\mathrm{DSI}}} x(t)\mathrm{d}t\right), \tag{1}$$

where P_i is the final pixel value, τ is the time spent to transfer the charge to the sensing node after the pedestal level has been measured, A is an arbitrary gain of the video chain, and $t_{i,\mathrm{DSI}}$ is the integration time. The first integral represents the integration over the charge and the second over the pedestal. The integrals are normalized by the integration time $t_{i,\mathrm{DSI}}$. The DSI can also be seen as a filter[3] with a frequency-domain transfer function

$$|H_{\mathrm{DSI}}(f)| = \frac{2A}{\pi t_{i,\mathrm{DSI}} f}\sin^2(\pi t_{i,\mathrm{DSI}} f). \tag{2}$$

The transfer function can then be used to evaluate the effect of the electronic noise sources after the read-out chain. The output noise power spectrum (S_{yy}) is equal to the input noise power spectral density (S_{xx}) times the square of the magnitude of the transfer function of the read-out system,[29] in this case $|H_{\mathrm{DSI}}(f)|$

$$S_{yy} = S_{xx}|H_{\mathrm{DSI}}(f)|^2. \tag{3}$$

Figure 5 shows the magnitude of the DSI filter $|H_{\mathrm{DSI}}(f t_T)|$ as a function of the normalized frequency $f \times t_T$ using the total pixel time $t_T = 2t_{i,\mathrm{DSI}}$ with $\tau = 0$. The X-axis has dimensional

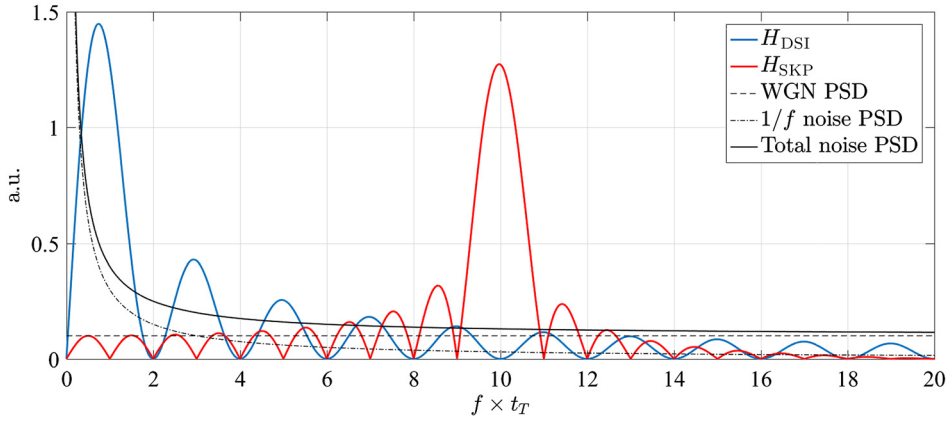

Fig. 5 Readout transfer function for the DSI used in standard readout systems (blue curve) and for Skipper-CCD for $N = 10$ (red curve) in arbitrary units. An example of the typical spectral behavior of the noise in the video signal (black) is also shown.[30]

units and can be scaled for any integration time of the DSI. The filter bandpass is maximum at a frequency of $f \times t_T = 1$. Since the numerator is bounded and periodic and the denominator is proportional to f, the filter attenuates high frequencies. At low frequencies, the filter response decays toward zero gain, again filtering the WGN flat spectrum. However, using Taylor expansion and the L'Hopital's rule, it can be shown that as f approaches zero, the integral of the $1/f$ noise is constant and independent of the integration time. Figure 5 also shows the spectral shapes of WGN, $1/f$ noise, and the combinations of both, which results in a typical noise spectrum present in the video signal at the input of the DSI.

DSI is optimal only for WGN because the standard deviation approaches 0 as the integration time goes to ∞. Non-WGN noise, such as $1/f$ low-frequency readout noise and other nonwhite system-level read-out noise, has remained a fundamental limitation for precision single-photon and single-electron counting in CCD-based systems. In conventional scientific CCDs, low-frequency readout noise results in rms variations in the measured charge per pixel at the level of $\sim 2\ e^-_{\mathrm{rms}}/\mathrm{pixel}$.[7,24,27,31,32] For longer integration times, the noise plateaus or even starts raising.

Similar results are obtained assuming a DDSI as is the case for the LTA. In this case, the integration time should be seen as the number of ADC samples (n_i) being average multiplied by the ADC sampling time ($T_S = 1/F_S$), $t_{i,\mathrm{DSI}} = n_i T_S$.

3.3 *Skipping Readout to Overcome 1/f Barrier*

A Skipper-CCD has a floating gate sensing node that allows multiple nondestructive measurements of the same pixel charge to be averaged in an uncorrelated fashion, breaking the $1/f$ dependence. In this case, the final pixel value is[11]

$$P_i = \frac{1}{N}\sum_{j=0}^{N-1}\frac{1}{t_{i,\mathrm{SKP}}}\left(\int_{t_{i,\mathrm{SKP}}+\tau+t_j}^{2t_{i,\mathrm{SKP}}+\tau+t_j} x(t)\mathrm{d}t - \int_{t_j}^{t_{i,\mathrm{SKP}}+t_j} x(t)\mathrm{d}t\right), \tag{4}$$

where t_j is the initial time of each measurement of the pixel charge and can be computed as $t_j = j(2I_{i,\mathrm{SKP}} + \tau + \psi)$, where ψ models any dead time between consecutive pixel measurements. A detail description of this Skipper sensors can be seen in Ref. 11. The corresponding transfer function magnitude (from Ref. 11) is

$$|H_{\mathrm{SKP}}(f)| = \frac{2A}{\pi N t_{i,\mathrm{SKP}} f}\sin^2(\pi t_{i,\mathrm{SKP}} f)\left|\frac{\sin(2\pi N t_{i,\mathrm{SKP}} f)}{\sin(2\pi t_{i,\mathrm{SKP}} f)}\right|. \tag{5}$$

The main advantage of the Skipper-CCD read-out system is revealed when its frequency response is compared to the standard DSI frequency response for the same total integration time (t_T), i.e., using the same total amount of time for all the samples in the Skipper readout $t_T = 2t_{i,\mathrm{DSI}} = 2Nt_{i,\mathrm{SKP}}$ assuming $\tau = \psi = 0$. In Fig. 5, the frequency response $|H_{\mathrm{DSI}}(ft_T)|$ of the DSI readout system is compared with $|H_{\mathrm{SKP}}(ft_T)|$ for $N = 10$. Both systems achieve the same level of white noise reduction because the total integration time t_T of the video signal is the same in both cases. However, the gain of Skipper-CCD readout system is much lower than that of the DSI readout system at low frequencies, allowing a readout noise reduction in the presence of low-frequency noise. This reduction can be increased by merely augmenting the number N of averaged samples. In other words, low-frequency noise filtering is achieved and the noise limitation is removed, at the expense of increasing readout time. This expectation has been extensively proven in Refs. 10 and 11.

Many combinations of integration times ($t_{i,\mathrm{SKP}}$) and number of measurements per pixel (N) can be used to obtain a desired overall read-out noise of the system. Their best values should be optimized based on the application and experimental setup. For example, in Ref. 11, the authors show how the optimization is performed to minimize the effect of both read-out noise and dark current contributions at the same time. For the purpose of this article, the performance of the LTA will be shown for several scenarios of $t_{i,\mathrm{SKP}}$ and N.

3.4 *Conversion Factor for Equivalent Noise Charge Measurements*

Gain calibration of the video signal chain plays a significant role in the normalization of the noise quantities referred to the charge signal being measured. Typical gain calibration procedures using x-rays or the photon transfer curves[3] rely on large charge packets of values per pixel, which rely on a very well-known mean ionization energy for x-rays at a given temperature and a uniform exposure for the photon transfer curve. To avoid any systematic error from these procedures, in this article, gain calibration is performed exploring the single charge counting capability of the Skipper-CCD. Using deep subelectron read-out noise levels, the pixel value can be fully discretized to an integer number of collected carriers. This enables an absolute and very precise calibration of the gain of the video chain as the difference between the pixel values of charge packets differing in one collected electron. This allows for a precise calibration in the entire dynamic range of the system. In Sec. 5, we exploit this capability to calibrate our system using pixels with zero and one collected electrons.

4 Intrinsic Noise Performance of the LTA

This section looks at the LTA electronics disconnected from the CCD and investigates: the noise characteristics of the interface electronics used to connect the LTA to the sensor; the noise at the LTA input given by the preamplifier, ADC, and all coupled noise from the rest of the board; the noise generated by the LTA control and bias lines.

4.1 *Noise Performance of the Interface Electronics*

The typical interface electronics used to connect the LTA to the sensor is a two-stage preamplifier (Fig. 6). The first stage must decouple the CCD dc bias while keeping a zero close to dc to avoid signal and pedestal drooping. At the same time, the noise added by that stage must be minimized. This is accomplished with the OPA209 in noninverting configuration. The nominal gain of the stage is 5, but lower or larger values are possible to adjust the dynamic range. A high-frequency pole is introduced on the feedback loop to minimize the output noise. The output noise spectrum referred to the input obtained using TINA (Toolkit for Interactive Network Analysis) Spice simulator is depicted in Fig. 7. At room temperature, the $1/f$ noise contribution at 100 Hz referred to the input is smaller than the typical noise of the CCD's video transistor.[11] The WGN floor is around $\sim$12 nV$/\sqrt{\text{Hz}}$, which, when referred to the input, is around $\sim$2.5 nV$/\sqrt{\text{Hz}}$, an order of magnitude lower compared to the $\sim$20 nV$/\sqrt{\text{Hz}}$ of the CCD MOSFET.[11] The noise spectrum shows a knee at about 1 MHz given by the high-frequency pole to minimize the total noise. A simulation of the noise contribution of the interface electronics noise in the DSI filtering

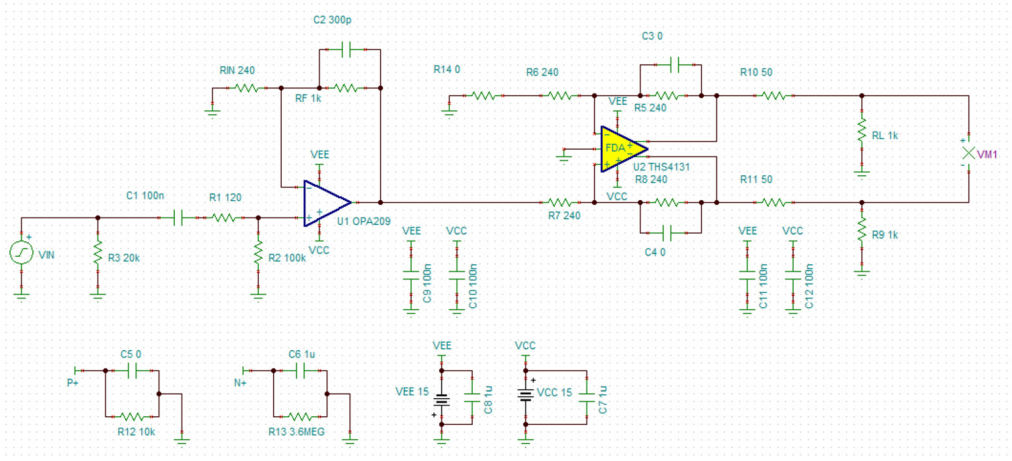

Fig. 6 Interface electronics schematic.

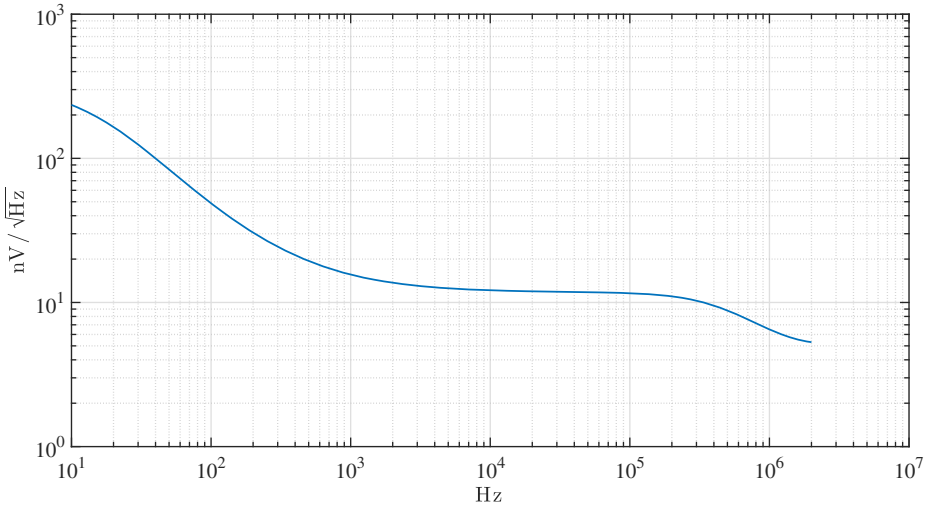

Fig. 7 Simulated interface electronics noise spectrum.

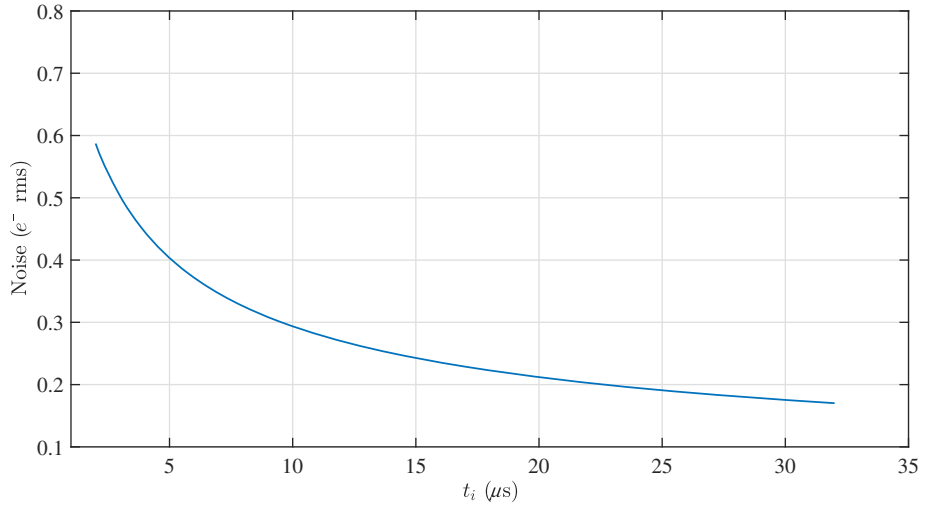

Fig. 8 Simulated interface electronics noise after DSI. As observed, the noise contribution by this stage is lower than one electron for all the integration times.

is shown in Fig. 8. For all integration times t_i, the noise is a fraction of one electron. The plot has been calibrated in electrons using a measured 2.5 μV/e$^-$ gain.

The purpose of the second stage is to convert the signal to differential output to reject common mode noise coupling on long cables running from the Dewar to the LTA electronics. Those cables are not needed for the current setup, but they will be needed for multi-CCD applications, for example, in experiments such as SENSEI that will have 50 CCDs and a total of 200 video channels, requiring 50 LTA boards.

4.2 *Noise Performance of the LTA*

A measurement of the noise of one of the the four LTA video inputs when terminated by a 50 Ω load is shown in Figs. 9 and 10. This load is equivalent to the output impedance of a low noise preamplifier located in the interface electronics, near the CCD (e.g., the CCD package or flex cable). The rest of the signals, bias, and clocks are loaded with *R-C* networks to emulate a CCD.

Figure 9 shows the noise spectrum when the clocks are held constant at nominal readout levels. The spectrum is $1/f$ dominated up to 10 kHz and is WGN until it finds the filter's pole located close to 1 MHz. The rms of the noise for a 1-MHz bandwidth is 20 μV at the input of the

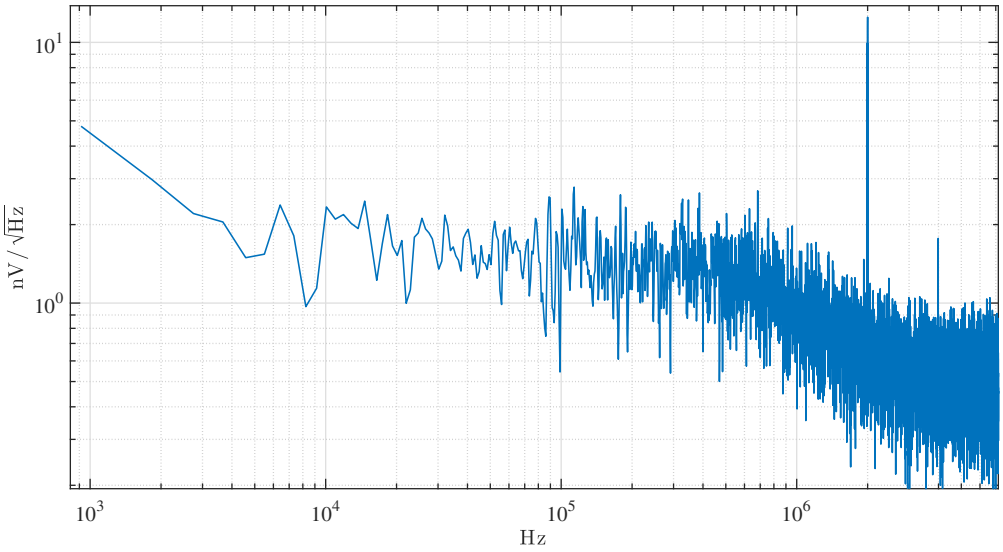

Fig. 9 Measured noise spectrum of the LTA using a 50 Ω terminated video channel.

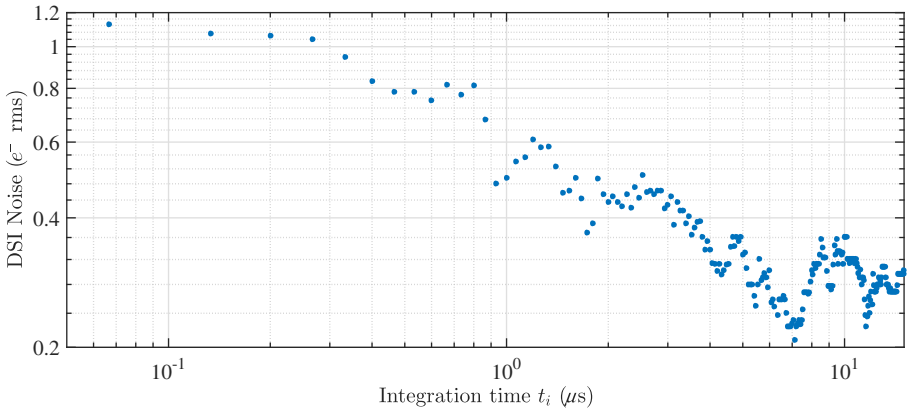

Fig. 10 Noise as a function of the integration time t_i at the output of the DSI using the 50 Ω terminated video channel.

LTA and represents 2.5 ADC counts when the internal preamplifier gain is 4. We typically use a transition preamplifier stage between the CCD and the LTA with a gain between 5 and 10. For a preamplifier gain of 10, the LTA noise referred to the input of the transition preamplifier (i.e., the CCD video output) is 2 μV rms. This rms noise is smaller than 1 electron when integrated by the DSI algorithm, becoming negligible.

Figure 10 shows the DSI noise as a function of the integration time (t_i) referred at the input of the interface preamplifier and with all the clocks switching as in a normal readout operation.

The CCD control and bias are sources of noise (Fig. 4). That noise capacitively couples to the video through the CCD and in the CCD package and cables. High $\frac{dV}{dt}$ noise has a bad impact in the noise, particularly during the read-out integration times. Figure 11 shows the noise spectrum of one of the LTA bias signals and one of the clock signals. Since all the bias use the same dc/dc converters, filters, and low dropout, that spectrum is representative for all biases. The same happens with the other clock signals, the spectrum shown is representative of the entire group. Both spectra show a flat WGN floor of $\sim$2 nV/$\sqrt{\text{Hz}}$. The $1/f$ noise meets the WGN at $\sim$30 kHz and its power is similar to the $1/f$ noise power of the internal video transistor (i.e., source follower of the CCD). However, only a small fraction of the bias and clock noise will couple to the video lines due to the CCD read-out circuit common mode rejection ratio (CMRR). The coupling of noise to the CCD package and cables is mostly capacitive. Henceforth, it is more important at higher frequencies and larger $\frac{dV}{dt}$. The spectra of Fig. 11 show tall lines of up to 20 dB higher than

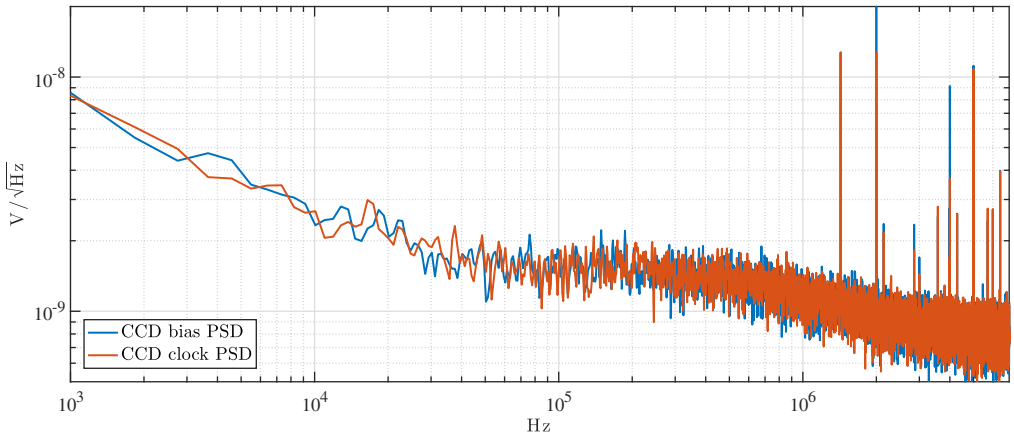

Fig. 11 Noise spectrum of the analog signals controlling the sensor.

the noise floor. These lines correspond to the dc/dc converter switching frequencies 2 MHz and harmonics. There are also smaller lines corresponding to internal oscillators for the digital electronics, mainly the FPGA. These lines are partially rejected by the 1-MHz analog filters at the interface electronics preamplifier and at the LTA preamplifier, but most importantly by the DSI. For a typical integration time of 10 μs the DSI attenuates a 2-MHz spike by more than 40 dB, making noise contribution above 2 MHz negligible.

To reject pick-up noise along the cables and noise coupled from the Dewar, the interface electronics and LTA input preamplifiers are differential. The CMRR of each stage is above 60 dB for frequencies above 1 MHz.

5 Noise Performance of the LTA with a Skipper-CCD

In this section, we discuss the performance of the LTA operating a Skipper-CCD.

5.1 *Readout Setup*

The experimental setup with a Skipper-CCD is shown in Fig. 12. The Skipper-CCD is built in silicon with a resistivity of 18 kΩ-cm, an active area of 9.216 cm $\times$ 1.329 cm, and a thickness of 675 μm. The sensors were designed at the Microchip Labs in LBNL. No thinning process was

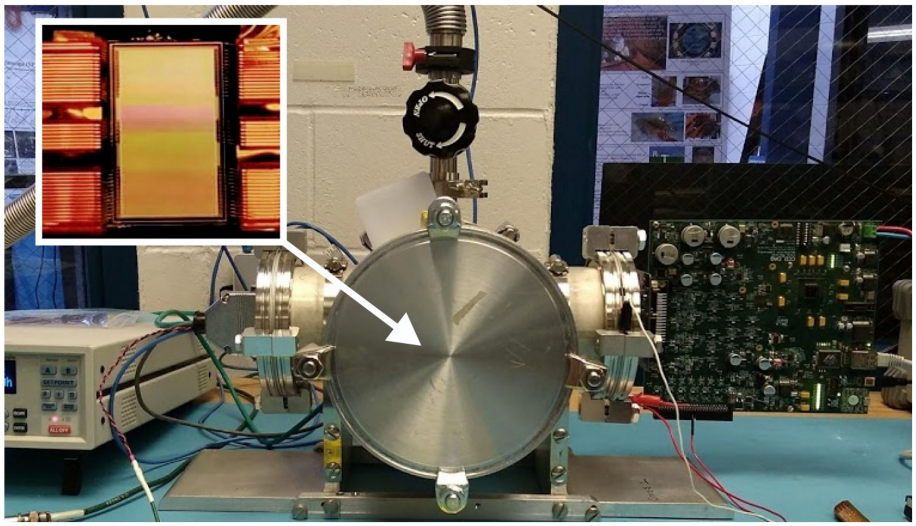

Fig. 12 Skipper-CCD setup with LTA electronics.

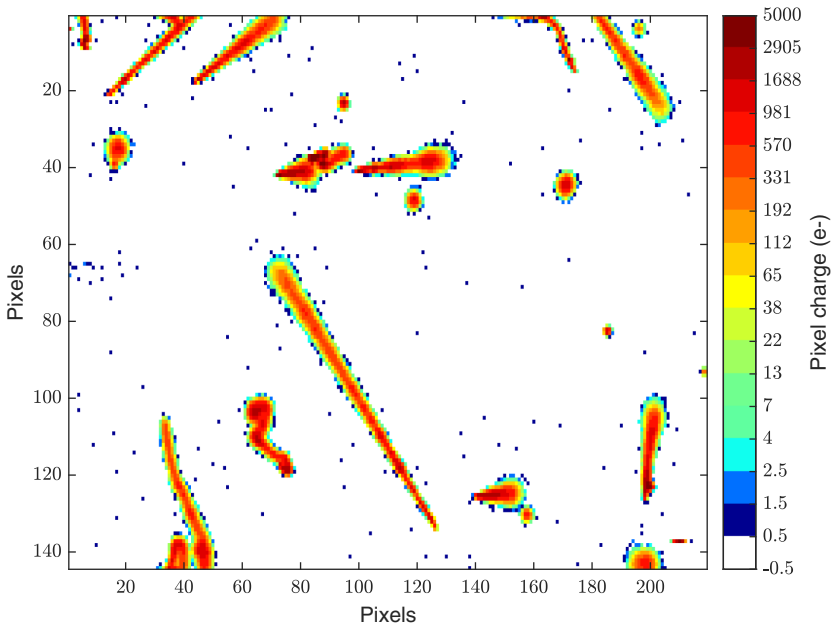

Fig. 13 Small portion of an output image when reading the sensor with deep subelectron noise level (0.15 e^-).

applied to the back side. The CCD has four identical amplifiers, one in each corner. Each amplifier can read the entire CCD, but the usual mode of operation is to read one quarter of the CCD containing 3072 rows and 443 columns of pixels. Each pixel has an area of 15 μm × 15 μm. A silicon pitch adapter is glued to the sensor and held in a copper box. A Kapton flex cable wire-bonded to the pads of CCD provides signal connectivity. The CCD was operated at a temperature of 135 K. The cooling system is based on a closed-circuit helium-based cryocooler. A cold finger penetrates the Dewar and connects to a copper mass on which the CCD sits flat. A temperature control system with a 50-W heater is used to keep the temperature of the CCD constant. Prior to cooling, the Dewar achieves vacuum (e.g., 10^{-5} torr) using a turbo vacuum pump. The flex cable ends in a DB-50 connector that connects to the interface electronics. The interface electronics connects directly to the 50-pin vacuum feed-through connector. The LTA connects to the outside part of the 50-pin connector. The vacuum and cooling lines are electrically isolated from the CCD system signal ground to avoid injecting low-frequency noise into the CCD read-out system. The LTA powers from +12 V dc (upper right corner of Fig. 12) and connects to the PC through an Ethernet cable (bottom right corner of Fig. 12). The data acquisition (DAQ) software runs on the PC and generates images in FITS file format. The DAQ can also control parameters (e.g., voltages and timing) and get status through the on-board telemetry. Figure 13 shows a portion of one of the images taken with the system. The CCD was exposed for 6 h in complete darkness. The color scale shows the charge of each pixel. The colors for the lower values of charge are exaggerated to clearly visualize pixels with fewer than four electrons. The image shows that there is no error in identifying pixels with no charge from those with charge. Single electrons in single pixels represent the dark current contribution of charge in the sensor. The long traces are mostly atmospheric Muons crossing the detector. The wiggling track is the ionization of a high-energy electron. The good energy resolution can be also observed in the edges of these high-energy events where only just a few electrons are observed.

5.2 *Gain Calibration*

The single charge counting capability of the Skipper-CCD was used to measure the gain of the video stage of each quadrant of the CCD. As was explained, the pixels are measured with deep subelectron noise so that the charge of each pixel can be determined unequivocally. Figure 14 shows the histogram for pixels with zero and one electron collected. Well-defined peaks are

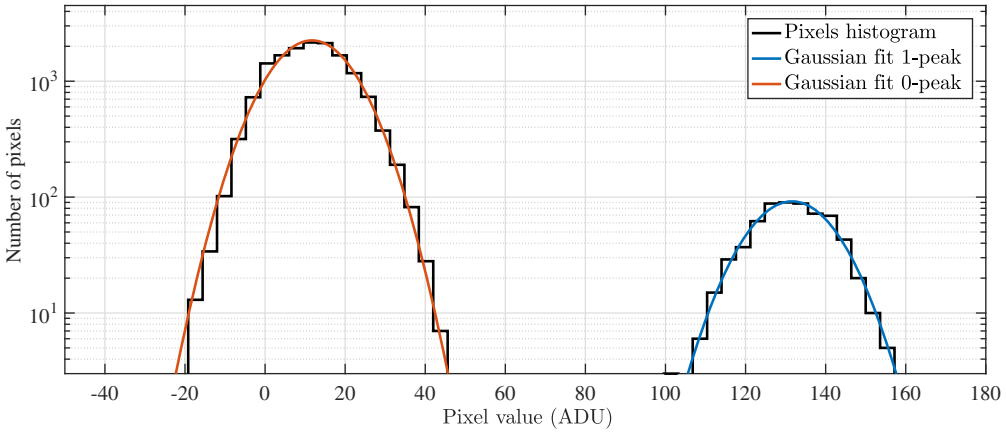

Fig. 14 Pixel histogram showing the zero and one electron peak for an integration time of $t_i = 8$ μs. The solid lines show the best fit to each of the peaks. The pixel values are shown in ADUs. The difference between the mean of each of the fits is used to calibrate the system and obtain the gain in ADU/e$^-$.

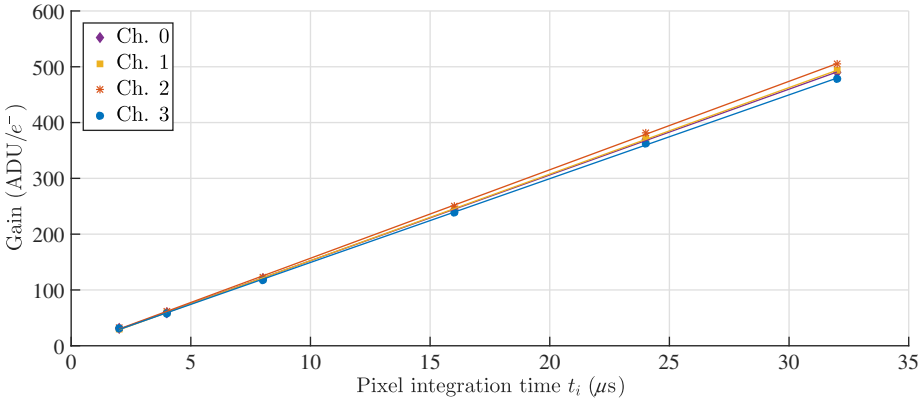

Fig. 15 Markers show the measured channel gain as a function of the pixel integration time t_i. The minimum square error fit for each channel is also shown revealing the linearity of the gain with t_i.

observed due to charge quantization. The measure of the difference of the mean between two consecutive peaks gives the relation between analog-to-digital-converter units (ADUs) and electrons of the entire signal video chain. The best normal fit to the peaks is used to estimate the gain as the difference of the fitted mean values.

The same procedure was repeated for the four amplifiers. The obtained gains of the system are shown in Fig. 15 as a function of the integration time (t_i) of the individual measurement of each pixel. The integration time t_i is the time interval during which the samples of the video signal are averaged to obtain either the pedestal or signal level. The solid lines in Fig. 15 are minimum-square-error fits of a straight line to the points, which show a linear and predictable response of the system.

5.3 *Integration Time Scan*

The read-out noise as a function of the integration time t_i is a typical performance test of any CCD camera system. For this experiment, only one Skipper sample $N = 1$ is used. Markers in Fig. 16 show the result of the noise scan measurements using the four channels. As expected, the noise is reduced when t_i is increased achieving around 2.5 electrons of noise for the higher values.

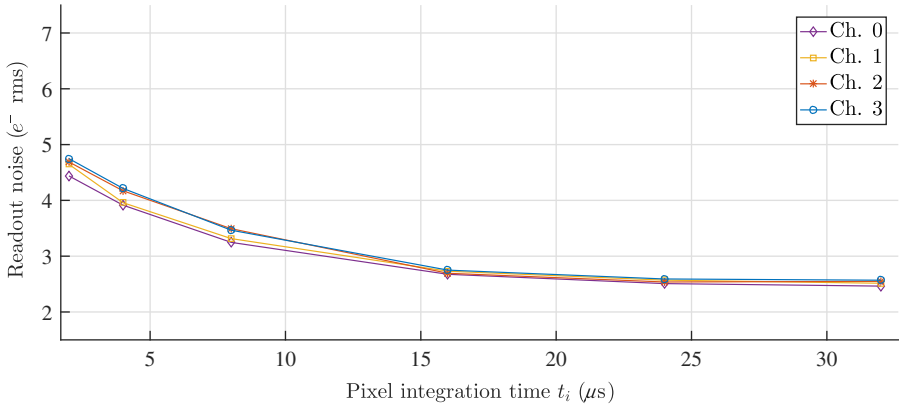

Fig. 16 Noise scan measurement. Noise of the setup measured in electrons as a function of the pixel integration time t_i. The integration time t_i is defined as the time during which the samples of the video signal are averaged to obtain either the pedestal or signal level.

5.4 *Skipper Scan and Gaussianity of the Readout Noise*

In this section, we present the experimental results of the readout noise for a sweep of the number of measurements N taken for each pixel. Given that the capability of taking multiple, nondestructive, independent samples of the same pixel charge is possible using the Skipper-CCD, we call this experiment a Skipper scan. Each sweep is computed for a fixed pixel integration time t_i.

The ability of the system for acquiring images that contain subregions with different number N of samples per pixel is used for this measurement. Images with seven different regions with $N = 1,10,50,100,500,1000,5000$ samples are used. Each subregion for a fixed N has around 650 pixels, several images are acquired so that tens of thousands of pixels are used to compute each measurement of noise, most of those pixels are empty with no charge in it.

To compute the Skipper scan, a basic and standard processing of the images is performed for each of the subregions corresponding to a fixed value of N. First, the mean is removed: if P_i^j is the original value of the i'th pixel from the j'th image then

$$\hat{P}_i^j = P_i^j - \overline{P}^j, \tag{6}$$

is the value of each pixel with the mean $\overline{P}^j$ of the subregion removed. The mean $\overline{P}^j$ is computed with all the pixels of the same image and subregion of N, discarding possible outliers values caused by unwanted charge in those pixels. The outliers are identified as pixel with more than three times the normalized median absolute deviation. In the second step, the baseline of the images is removed. To perform this operation, the median M of the images is computed and subtracted to each of the images and if M_i is the i'th pixel of the median, then

$$\tilde{P}_i^j = \hat{P}_i^j - M_i \tag{7}$$

is the i'th pixel of the j'th image with the mean and baseline removed. The $\tilde{P}_i^j$ pixels of the same subregion of all the images are collected together and used to compute the noise of the system.

Figure 17 shows the results of the Skipper scan test. The Skipper operation corresponds to averaging N independent noise sources (empty pixels, which do not have charge), which results in a reduced read-out noise. This reduction is theoretically proportional to $1/\sqrt{N}$ and becomes a straight line in a log–log plot, which is also shown in Fig. 17 with solid lines. To estimate the proportionality constants $n_0 \ldots n_3$ for each channel, indicated in the legend of Fig. 17(a), least squares minimization using the points of each channel was applied. Figure 17(a) depicts the noise in electrons as a function of N for the four channels available in the system and for an integration time of the pixel of $t_i = 32$ μs. The experimental data are indicated with markers (diamonds, squares, asterisks, and solid circle). This plot reveals that all channels are almost superimposed, indicating that the noise performance of all the channels is the same, which is a desirable property. It can also be observed that the measurements follow the predicted rate

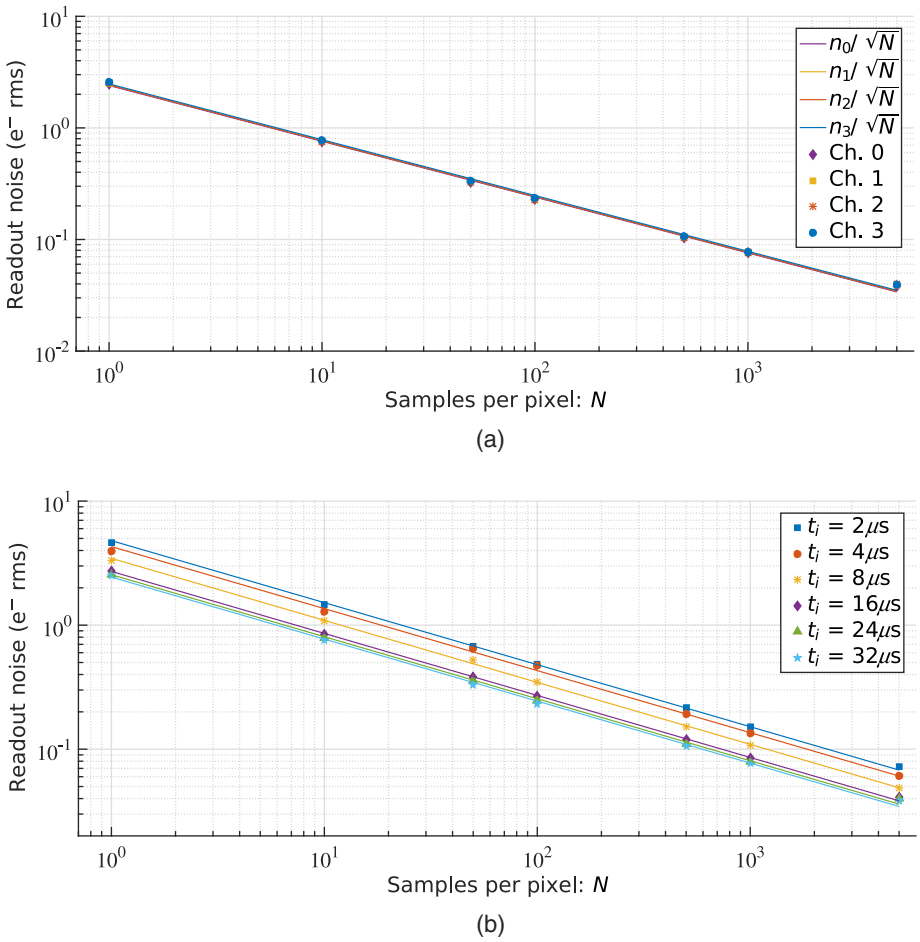

Fig. 17 Skipper scan measurements: sweep of the read-out noise as a function of the number of samples N taken for each pixel. (a) The Skipper scan for the four channels and an integration time of the pixel of $t_i = 32$ μs; (b) the Skipper scan for only one channel parametrized for different integration times of the pixel: $t_i = 2,4,8,16,24,32$ μs. In both figures, measurements are indicated with markers and the straight lines show the theoretical prediction $\propto 1/\sqrt{N}$.

of noise reduction as a function of N. The lower noise is achieved for $N = 5000$ and is around 0.039 e^-_{rms}/pix.

Figure 17(b) shows the results of the Skipper scan for channel 1 using different pixel integration times: $t_i = 2,4,8,16,24,32$ μs. Parallel lines following the theoretical $\propto 1/\sqrt{N}$ prediction are observed in all cases. In agreement with results in Sec. 5.3, the noise reduction (separation between lines) is more significant when increasing t_i for the lower values, for example, when increasing the integration time from $t_i = 4$ μs to $t_i = 8$ μs, and reaches a plateau for higher values of t_i, for example when increasing from $t_i = 16$ μs to $t_i = 24$ μs or $t_i = 24$ μs to $t_i = 32$ μs. This is the expected behavior as the noise scan shows in Fig. 16.

Figure 18 shows the pixel histogram (in log scale) corresponding to the parameters $t_i = 32$ μs and $N = 5000$. The peaks at 0 electrons and 1 electron were obtained by fitting a normal distribution to the data. The estimated standard deviation is the square root of the unbiased estimate of the variance. The logarithmic scale reveals that the data follow the normal fit over more than 4 orders of magnitudes showing the Gaussianity of the readout noise in a wide range, which is also a desirable property.

This characteristic is still valid for pixels with a large amount of charge collected. The histogram shown in Fig. 19 was obtained from a set of exposures to an LED light. It is still possible to observe the Gaussian and extremely low noise in pixels with hundreds of electrons. The maximum full well capacity of similar high resistivity CCD with the same pixel size has been proven to be greater than 10^5 electrons by the authors of this work.[33] The Skipper-CCD and the

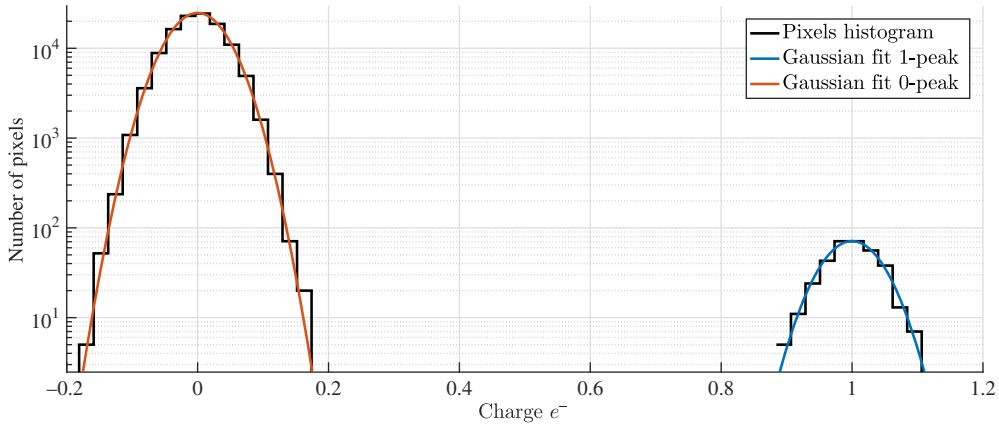

Fig. 18 Histogram of the pixels with charge in the range between $0e^-$ and $1e^-$ and Gaussian fit for peaks of 0 and 1 electron. The *y*-axis in logarithmic scale to show Gaussianity of the readout noise over more than 4 orders of magnitude. The histogram was computed for channel 2, an integration time of $t_i = 32$ μs, and $N = 5000$ samples for each pixel.

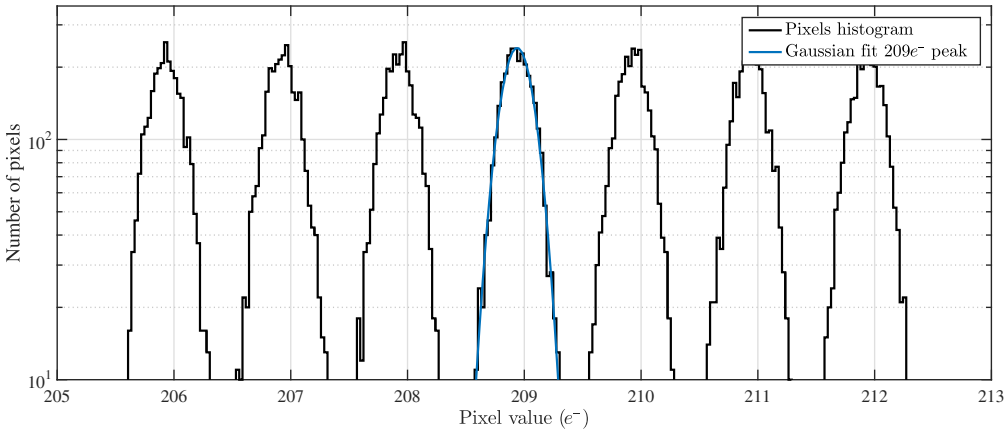

Fig. 19 Histogram of pixels with hundreds of electrons of charge. The blue curve is the Gaussian fit of the peak for pixels with 209 e$^-$,-. It has a σ of 0.13 e$^-$.

LTA were designed to be able to handle this charge range, obtaining a dynamic range of $20\log_{10}(10^5/1) = 120$ dB, which is defined as the ratio between the largest charge packet (10^5 electrons) and the lower charge packet (1 electron) to be readout.

6 Conclusion

In this work, the first controller for Skipper-CCD was presented. This type of CCD allows non-destructive readout of the same pixel charge multiple times, which reduces the readout noise. It was especially designed for high-sensitive applications requiring subelectron noise. With this new electronic controller, we achieved an unprecedented deep subelectron noise of 0.039 e^-_{rms}/pix by measuring and averaging the charge in each pixel 5000 times. The controller is a fully digital, single board, four-channels, Ethernet-based system, which provides the necessary signals and sequencing flexibility. A detailed description of the main components and functionalities of the system were presented. The results from standard CCD tests were detailed to show its performance.

Acknowledgments

Part of this research has been financed by Grants 24/K078 and 24/K090 (Sgcyt-UNS), and PICT-2016-4825 (FONCYT-Agencia). The CCD development work was supported in part by the

Director, Office of Science, of the U.S. Department of Energy under Contract No. DE-AC02-05CH11231.

References

1. W. S. Boyle, "Nobel lecture: CCD-an extension of man's view," *Rev. Mod. Phys.* **82**, 2305–2306 (2010).
2. G. E. Smith, "Nobel lecture: the invention and early history of the CCD," *Rev. Mod. Phys.* **82**, 2307–2312 (2010).
3. J. R. Janesick, *Scientific Charge-Coupled Devices*, Vol. 83, SPIE Press, Bellingham, Washington, DC (2001).
4. DESI Collaboration et al., "The DESI experiment part II: instrument design," arXiv: 1611.00037 (2016).
5. K. Gilmore et al., "The LSST camera overview: design and performance," *Proc. SPIE* **7014**, 70140C (2008).
6. L. Barak et al., "SENSEI: direct-detection results on sub-GeV dark matter from a new Skipper CCD," *Phys. Rev. Lett.* **125**, 171802 (2020).
7. A. Aguilar-Arevalo et al., "Exploring low-energy neutrino physics with the coherent neutrino nucleus interaction experiment," *Phys. Rev. D* **100**, 092005 (2019).
8. J. J. Blostein et al., "Development of a novel neutron detection technique by using a boron layer coating a charge coupled device," *J. Instrum.* **10**, P01006 (2015).
9. J. Janesick, *Photon Transfer: DN [Lambda]*, SPIE Press, Bellingham, Washington (2007).
10. J. Tiffenberg et al., "Single-electron and single-photon sensitivity with a silicon Skipper CCD," *Phys. Rev. Lett.* **119**(13), 131802 (2017).
11. G. F. Moroni et al., "Sub-electron readout noise in a Skipper CCD fabricated on high resistivity silicon," *Exp. Astron.* **34**, 43–64 (2012).
12. B. M. Starr et al., "MONSOON: image acquisition system or 'pixel server'," *Proc. SPIE* **4841**, 600–611 (2003).
13. B. M. Starr et al., "MONSOON image acquisition system," in *Scientific Detectors for Astronomy*, P. Amico, J. W. Beletic, and J. E. Beletic, Eds., pp. 269–276, Springer, Dordrecht (2004).
14. R. W. Leach, "Design of a CCD controller optimized for mosaics," *Publ. Astron. Soc. Pac.* **100**, 1287 (1988).
15. R. W. Leach, "CCD controllers," in *New Developments in Array Technology and Applications*, A. G. D. Philip, K. A. Janes, and A. R. Upgren, Eds., pp. 49–56, Springer, Dordrecht (1995).
16. R. W. Leach and F. J. Low, "CCD and IR array controllers," *Proc. SPIE* **4008**, 337–343 (2000).
17. J. Estrada, "Observatory of kipper CCDs unveiling recoiling atoms," 2020, https://astro.fnal.gov/science/dark-matter/oscura/ (accessed 29 October 2020).
18. A. Aguilar-Arevalo et al., "Constraints on light dark matter particles interacting with electrons from DAMIC at SNOLAB," *Phys. Rev. Lett.* **123**, 181802 (2019).
19. J. C. D'Olivo et al., "vIOLETA: neutrino interaction observation with a low energy threshold array," in *XXIX Int. Conf. Neutrino Phys.*, poster 521 (2020).
20. D. Rodrigues et al., "Absolute measurement of the Fano factor using a Skipper-CCD," arXiv:2004.11499 (2020).
21. G. Fernandez-Moroni et al., "Charge collection efficiency in back-illuminated charge-coupled devices," arXiv:2007.04201 (2020).
22. K. Kuk et al., "A boron-coated CCD camera for direct detection of ultracold neutrons (UCN)," arXiv:1903.01335 (2019).
23. F. Chierchie et al., "Detailed modeling of the video signal and optimal readout of charge-coupled devices," *Int. J. Circuit Theory Appl.* **48**, 1001–1016 (2020).
24. S. E. Holland et al., "Fully depleted, back-illuminated charge-coupled devices fabricated on high-resistivity silicon," *IEEE Trans. Electron Devices* **50**, 225–238 (2003).

25. M. S. Haro et al., "A low noise digital readout system for scientific charge coupled devices," in *XVII Workshop Inf. Process. and Control*, IEEE, pp. 1–5 (2017).
26. G. F. Moroni et al., "Interleaved readout of charge coupled devices (CCDs) for correlated noise reduction," *IEEE Trans. Instrum. Meas.* **69**, 7580–7587 (2020).
27. M. S. Haro et al., "Measurement of the read-out noise of fully depleted thick CCDs," in *Argentine Conf. Micro-Nanoelectron., Technol. and Appl.*, IEEE, pp. 11–16 (2016).
28. G. F. Moroni et al., "Low threshold acquisition controller for Skipper charge coupled devices," in *Argentine Conf. Electron.*, pp. 86–91 (2019).
29. A. Papoulis, *Probability and Statistics*, Prentice-Hall International Editions, Prentice Hall (1990).
30. J. Jaeckel and S. Roy, "Spectroscopy as a test of Coulomb's law: a probe of the hidden sector," *Phys. Rev. D* **D82**, 125020 (2010).
31. A. Aguilar-Arevalo et al., "Search for low-mass WIMPs in a 0.6 kg day exposure of the DAMIC experiment at SNOLAB," *Phys. Rev. D* **D94**(8), 082006 (2016).
32. M. Haro et al., "Taking the CCDs to the ultimate performance for low threshold experiments," Tech. Rep., Fermi National Accelerator Lab. (FNAL), Batavia, Illinois (2016).
33. J. Estrada et al., "Focal plane detectors for dark energy camera (DECam)," *Proc. SPIE* **7735**, 77351R (2010).

Biographies of the authors are not available.